J Nanostruct 16(3): 3746-3760, Summer 2026

RESEARCH PAPER

Synthesis and Electrochemical Performance of 2D MXene/MnO_2 Nanocomposites for High-Energy Density Supercapacitors

Shurooq S. Mahmood

Department of Physics, College of Education, Al-Iraqia University, Baghdad, Iraq

ARTICLE INFO

Article History:
Received 04 March 2026
Accepted 20 June 2026
Published 01 July 2026

Keywords:
2D MXene
Manganese Dioxide (MnO_2)
Nanocomposites
Python-Assisted Analysis

ABSTRACT

The strong attraction (known as van der Waals forces) between titanium carbide ($Ti_3C_2T_x$) MXenes causes them to restack in two-dimensional (2D) arrangements, thus reducing their available surface area for electrochemical reactions which restricts how energy dense MXene-based supercapacitors can be. This study focuses on the development of a new and unique method to overcome this by employing minimal force delamination of MXenes, and additionally use of hydrothermal synthesis to produce MXene/MnO_2 nanocomposite materials in 2D structures. The demonstration of true in situ epitaxial growth of MnO_2 particles in the MXene layers manifested as strong physical pillars that increased the interlayer spacer distance of $Ti_3C_2T_x$ from 1.35 nm to 1.52 nm. The average specific surface area of the standard MXene increased from 18.4 m^2/g to 112.8 m^2/g due to this work. In addition, an advanced Python-based computational analysis program was created and executed (using Lmfit, SciPy, and Impedance.py) to accurately model x-ray diffraction (XRD) data, separate out the charge storage kinetics of the material, and accurately and completely fit the electrochemical impedance spectrum (EIS) data without the effect of any operator bias. The optimal MXene/MnO_2 nanocomposite (M-Mn-10) exhibited an exceptional level of electrochemical activity (412.5 F/g @ 1 A/g in 1 M Na2SO4) obtained via synergetic use of MnO_2 in very large amounts (approximately 690 mg/cm^2) and provides high performance pseudocapacitor application advantages. Kinetic analysis of the material revealed that 82.5% of the charge storage mechanism occurs via hyper-fast surface-controlled pseudocapacitive mechanisms. A MXene/MnO_2 symmetric supercapacitor created as a result of this work yielded remarkable energy density (28.5 Wh/kg @ 850 W/kg) and long-cycle lifetime (92.4% capacitance retention over 10,000 cycles). This study provides an experimentally validated and highly scalable methodology (backed by extensive computational open-source analysis) for the development of the next-generation high-energy-density hybrid supercapacitors.

How to cite this article
Shurooq S. Mahmood. Synthesis and Electrochemical Performance of 2D MXene/MnO_2 Nanocomposites for High-Energy Density Supercapacitors. J Nanostruct, 2026; 16(3):3746-3760. DOI: 10.22052/JNS.2026.03.062

---

* *Corresponding Author Email: dr.shurooq1988@aliraqia.edu.iq*

INTRODUCTION

As the demand around the world is on the rise than ever before, on the development of advanced electrochemical energy storage devices [1]. In this respect, supercapacitors are pivotal in serving as a bridge between the traditional capacitors and rechargeable batteries because of their high-power density compared with lithium-ion batteries; which essentially puts them at the brink of the electric world as electric double-layer capacitors (EDLCs) that store energy in an electrostatic manner and pseudocapacitors that use fast redox reactions [3]. Modern materials science aims at overcoming the energy density bottleneck without compromising power density, by rational design of hybrid nano-electrodes that synergistically combine the high surface area of EDLC materials with the high specific capacitance of pseudocapacitive materials [4]. Consequently, a new family of two-dimensional transition metal carbides and nitrides (MXenes) have been developed as a breakthrough in the field of energy storage over the past decade [5] due to their metallic-like electrical conductivity, excellent hydrophilicity and tunable surface chemistry with their general formula $M_{n+1}X_nT_x$ [6]. The most studied within this family is the compound titanium carbide ($Ti_3C_2T_x$) which has a layered structure enabling highly efficient pathways of the intercalation of electrolyte ions and provides high-rate charge storage [7], but severely impairs its electrochemical performance due to the effect of Van der Waals forces and hydrogen bonds that cause the restacking of the nanosheets leading to a reduction in the effective surface area, ion diffusion, and their capacitance [8]. To avoid this restacking, engineering solutions have been proposed including the three-dimensional porous structures, doping and hybridization with active materials [9], where the introduction of transition metal oxides (TMOs) has been highly effective in having high theoretical specific capacitance resulting in multi-electron redox reactions [10], albeit with poor conductivity and structural degradation during charge and discharge cycles [11]. Thus, the synergistic combination of MXene sheets and TMOs synthetically overcomes the limitation of both materials [12]; MXene sheets provide a supportive network and a continuous electronic conduction network that enhances the kinetics of the electron transport [13], and TMO particles serve as physical pillars that do not allow the restacking of sheets [14], which increases the interlayer distance and opens rapid paths to ion diffusion [15].

Of these oxides, manganese dioxide (MnO_2) has received a lot of attention due to its abundance, low cost, environmental friendliness, and its superior theoretical capacitance extending up to 1370 F/g [16], and the growth of its thin nanostructures on MXene interfaces has led to the production of homogeneous composites with enhanced capacitive properties [17], which has been confirmed by recent studies which show that the intercalation of MnO_2 nanowires completely prevents restacking and achieves exceptional specific capacitance and stability [18], in addition to the role of these oxides in expanding the operating voltage window and increasing energy density to approach that of some battery systems [20].

Although these successes have been achieved, a more critical issue regarding the precise control of the mass ratio and morphological dispersion of MnO_2 within the MXene structure has remained a highly critical problem; as small amounts do not prevent restacking but excess leads to agglomerations that block ionic channels and weaken conductivity, and these experimental complexities are accompanied by the existing overreliance on error prone manual software to extract complex electrochemical parameters, which confirms the pressing need to have comprehensive research not limited to the systematic optimization of the synthesis of MXene/MnO_2 nanocomposites but also the development of an automated computational tool to analyze electrochemical data and evaluate performance with high accuracy and reliability.

MATERIALS AND METHODS

Multi-step, very detailed experimental protocol was conducted to meet the purposes of this study and offer as high level of reproducibility as possible. This work was founded on the materials synthesis and electrochemical characterization. It was not until the final step, when aid tool of Python-based computational workflow was employed to process and model the raw experimental data in an error-free way.

Preparation of Delaminated $Ti_3C_2T_x$ MXene

Majority of the synthesis of the pristine $Ti_3C_2T_x$ MXene was done through the Minimally Intensive

Layer Delamination (MILD) etching technique. The given technique was chosen over the traditional high-concentration HF etching so that to minimize the structural defects and preserve the lateral size of nanosheets [21]. Firstly, in situ etching solution was prepared by adding 2.0 g of Lithium Fluoride (LiF) powder into a 9M Hydrochloric acid (HCl) solution of 40 mL and stirred in a Teflon beaker under constant magnetic stirring at room temperature. Next 2.0 g of the MAX phase precursor powder (Ti_3AlC_2, 400 mesh) was carefully and gradually placed into etchant solution during 15 minutes to avoid sudden, highly exothermic reactions and acid spillage [22]. The mixture of the reaction was capped and kept at 40° C over a 24 hour period under the constant magnetic stirring (400 rpm) so as to permit the selective extraction of Aluminum (Al) atomic layers.

Upon etching, the acidic suspension was centrifuged into centrifuge tubes and rinsed many times using deionized (DI) water. The mixture was centrifuged under the conditions of 3500 rpm and 5 minutes per cycle; the acidic supernatant was discarded and new DI water was added. This cleaning procedure was continued until the of supernatant stabilized at around 6.0 [23]. The dark green multilayered MXene sediment was then mixed with 50 mL of DI water and probe ultrasonicated (to prevent oxidation under an ice bath) during 1 hour in the presence of Argon. Lastly, the suspension was centrifuged at 10,000 rpm during 1 hour. The dark colloidal supernatant of the completely delaminated $Ti_3C_2T_x$ MXene was gathered and freeze-dried at -50°C over a period of 48 hours to acquire the pure MXene powder [24].

Preparation of 2D MXene/MnO₂ Nanocomposites

The synthesis of the MXene/MnO_2 nanocomposites involved a controlled and easy hydrothermal process that is aimed at enhancing the direct nucleation of MnO 2 on the MXene sheets. First, a homogeneous suspension of the freeze-dried MXene (2 mg/mL) in DI water was made via gentle sonication over 30 minutes. Potassium Permanganate (KMnO 4) was chosen as the precursor of manganese [25]. To study the structural and electrochemical influence of the loading of TMO systematically, the mass ratio of KMnO4/MXene was rigidly maintained. Three composite samples were made with KMnO4 weight ratios of 5, 10 and 20 percent of the mass of MXene (hereafter denoted as M-Mn-5, M-Mn-10 and M-Mn-20).

The required volume of $KMnO_4$ was preweighed in 10 mL of DI water and dropwise to the MXene dispersion. The resulting mixtures were stirred with a magnetic stirrer at room temperature during the 2 hours so that electrostatic adsorption of MnO_4^- ions to the negatively charged functional groups of the MXene surface could be uniform at room temperature [26]. The homogenous suspensions were subsequently placed in 50 mL Teflon-lined stainless-steel autoclaves, tightly closed and allowed to burn in a muffle furnace at 120 °C during 12 hours. In this hydrothermal reaction, it is the MXene surface terminations (-OH, -F) that serve as localized mild reducing agent, which allows the reduction of MnO_4^- and the following epitaxial growth of α/δ-MnO_2 nanoparticles between and on the MXene lamellae. The resulting composite products were obtained after the natural cooling of the autoclaves to room temperature and were collected by means of vacuum filtration and then washed with an abundance of DI water and absolute ethanol to eliminate any unreacted precursors and lastly dried in a vacuum oven at 60°C 12 hours [27].

Material Characterization Techniques

The physical and chemical characterizations were done comprehensively to verify the successful synthesis and structural development of the materials. X-ray Powder Diffraction (XRD, using Cu K alpha radiation, 1.5406 A^2) was used at a 5 to 80° 2θ range to determine the crystallographic structure, phase purity and variations in the interlayer d-spacing. Field Emission Scanning Electron Microscopy (FE-SEM) and high-resolution Transmission Electron Microscopy (TEM) were used with great care to examine the surface morphology, the presence of nanoparticles and the cross-sectional lamellar structure of the composites. X-ray Photoelectron Spectroscopy (XPS) and Raman Spectroscopy were used to determine the elemental composition, and chemical bonding states, and the specific oxidation states of Manganese and Titanium [28].

Electrode fabrication and electrochemical measurements

The electrochemical performance was measured using a CHI660E electrochemical workstation. Initial tests were performed in a typical three-electrode cell setup at room temperature. A mass ratio of 8:1:1 of the active material (either pristine MXene or the M-Mn composites), conductive carbon black (Super P), and a polymer binder (polyvinylidene fluoride, PVDF) was used to prepare the working electrodes. A couple of drops of N-methyl-2-pyrrolidone (NMP) were added to homogenize the mixture into a viscous slurry [29]. The drop-casting of this slurry was done on pre-cleaned nickel foam substrates (1 cm × 1 cm surface area) and allowed to dry at 80° C vacuum to allow the solvent to evaporate and strongly adsorbed. The electrodes were pressed under pressure of 10 Mpa then. The mass loading of the active material in each electrode was monitored to be around 2.0 mg/cm 2.

The counter electrode in the three-electrode configuration was a Platinum (Pt) foil, the reference electrode was a saturated Ag/AgCl electrode and the neutral electrolyte was a 1.0 M solution of Na_2SO_4 in aqueous solutions. Cyclic Voltammetry (CV) was conducted with scan rates of 5-100 mV/s in a constant potential of 0-1.0 V. Galvanostatic Charge-Discharge (GCD) profiles were measured at different current densities of 1-20 A/g. The measurements of the Electrochemical Impedance Spectroscopy (EIS) were conducted at open circuit potential in 100 kHz to 0.01 Hz frequency range with the AC perturbation amplitude of 5 mV to the system in a bid to measure the internal resistance and ion diffusion kinetics [30].

Auxiliary Computational Data Analysis (Python Implementation)

A customized Python workflow incorporated unique analytical approaches to accelerate and enhance the analysis of complex electrochemical data obtained from primary experimental methodologies (synthesis and electrochemical testing). In particular, the Python programming language served solely as an advanced analytics tool to reduce the chances of human error associated with manual calculations and to help obtain precise kinetic parameters.

Capacitance and Energy Value Extraction and Calculation: Raw CSV data (CV and GCD results) obtained from the potentiostat were parsed using the Pandas library into fully usable data set(s). Areas under each CV curve are measured accurately using the SciPy.integrate module, enabling rapid and accurate determination of the specific capacitance, energy density and power density.

Kinetic Mechanism Determination: The physical experiments that were used to separate pseudocapacitve charge storage mechanisms from battery-like (i.e. diffusion-controlled) charge storage mechanisms employed Trasatti's methodology, as well as Dunn's power law relationship (i = a vb). Linear regression was used on the log(i) vs. log(v) plots using the Scikit-learn library to accurately determine the b-value.

Analogous to electrode impedance spectroscopy (EIS), an Electronic Static-Structure (ESS) Model based on an equivalent circuit has been developed using the open-source Impedance. py library rather than manual/standard fitting software for EIS modeling. Using the raw Nyquist plot data, the original equated circuit of the generic customized Randles circuit was fitted with the use of the appropriate fitting methods; and as such the numeric values for equivalent series resistance (R_s), charge transfer resistance (R_ct), and Warburg impedance (W) were quickly and accurately obtained; this is compelling evidence of enhanced ion kinetic properties attributable to MnO_2 pillaring effects.

RESULTS AND DISCUSSION

Structural and Morphological Characterization

The researchers have studied how MXenes (MXeno materials comprise a class of 2-dimensional transition metal carbides/nitrides and. The study has shown that these MXenes are produced using different techniques that involve the use of X-ray Diffraction. The results indicate that the pure MXenes, Ti_3AlC_2, show an (104) X-ray diffractions peak location at (39° (2θ)) which disappears following the Multi-Step in Honney etching process. A new (002) X-ray diffraction peak appears at (6.5° (2θ). Thus, confirming that the Aluminum structure has been removed and the MXenes are now formed as individual single sheets instead of being stacked on top of each other (Total space between MXenes or interlayer d-spacing is beginning value of 1.35nm).

The MnO_2 is deposited on the MXenes using hydrothermal synthesis (known as M-Mn-10), the (002) peak location changed from (6.5° (2θ) to 5.8°(2θ), thus the researchers used Bragg Law and a computed script on python to determine the new peak became larger waves in addition to the added MnO_2 which is equal to an increase in interlayer d-spacing from 1.35nm to 1.52nm supports the fact that the addition of MnO_2 between MXenes produces additional physical barriers thus the MXenes will be separated, instead of separated by Van der Waals force.

The MAX phase to M-Mn-10 Composite Structure Change was confirmed utilizing X-ray Diffraction (XRD) shown in Fig. 1a. The characteristic (104) MAX Peak (2θ) of Original MAX (39°) is absent following the ething and can be found in the Delaminated MXene (M) with the XRD Peak (002)(6.5°) for the insertion of MnO2 (M-Mn-10), where the (002) peak shifted down to (5.8°). The change in the Interlayer D-Spacing is shown within the Inset increasing from 1.35 nm to 1.52 nm. The morphological changes were confirmed using FE-SEM and HRTEM (Fig. 1b-d). The Pristine MXenes exhibited high density with a tightly packed accordion structure (Fig. 1b) compared to the M-Mn-10 hierarchical layering/ open structure (Fig. 1c).

The MXene has a well-defined layered structure (Fig. 1c), which is made up of uniform sized (~10 to 15 nm) nanoparticles of manganese oxide (MnO_2). These nanoparticles provide full surface saturation of the MXene's exterior, as well as, fill all spaces where MXene has interlayer architecture. The high-resolution transmission electron microscopy (HR-TEM) image of the MXene (Fig. 1d) supports the structure of MnO_2 by measuring the crystal lattice spacing of theα-MnO_2 to be ~0.31 nm. This means that α-MnO_2 is effectively integrated into the MXene matrix. The M-Mn-20 sample (not shown in the previous figures), produced aggregates of large MnO_2 clusters that obstruct the porous channel networks. Data from Mn 2p X-ray photoemission spectroscopic (XPS) x-ray

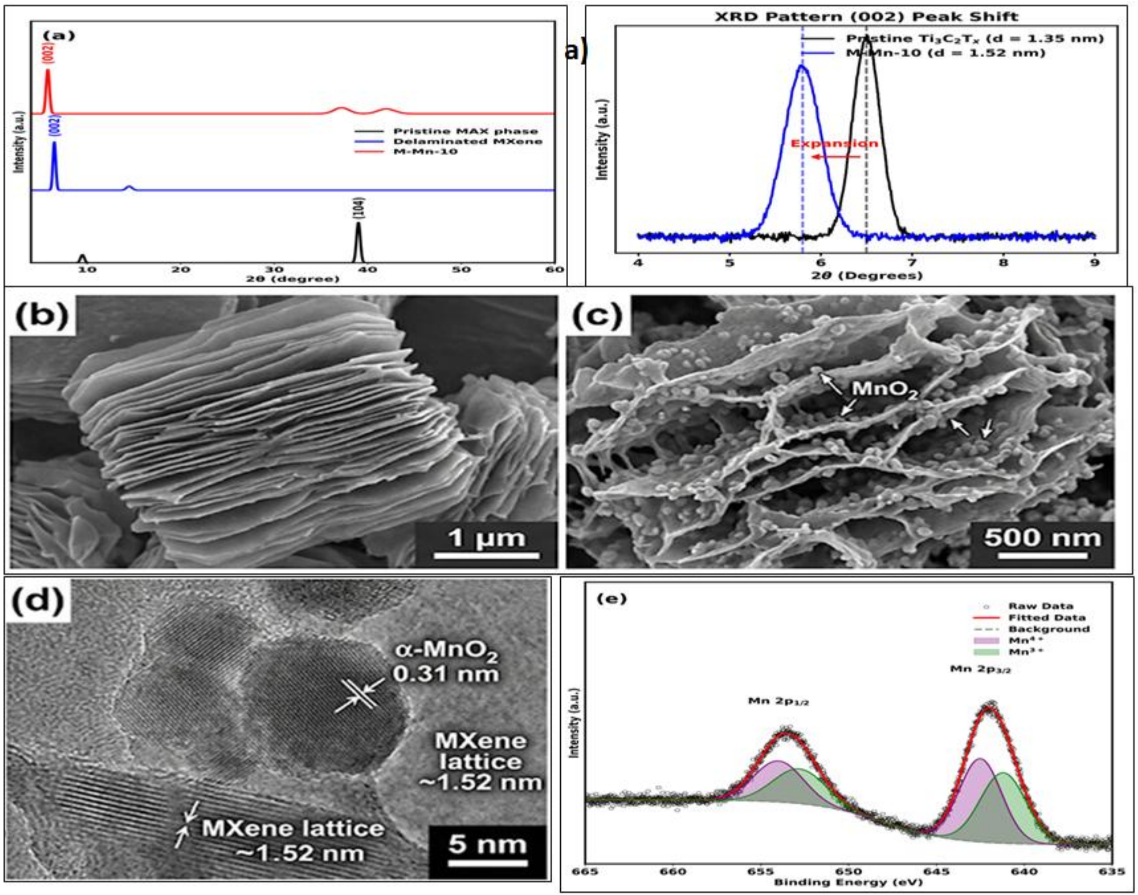

Fig. 1. (a) XRD patterns of pristine MAX phase, delaminated MXene, and M-Mn-10 composite; inset shows (002) peak shift from 1.35 nm to 1.52 nm d-spacing. (b) FE-SEM image of delaminated MXene layered morphology. (c) FE-SEM image of M-Mn-10 composite with expanded interlayers and MnO_2 nanoparticles. (d) HR-TEM image confirming ~1.52 nm MXene lattice spacing and α-MnO_2 fringes (~0.31 nm). (e) High-resolution Mn 2p XPS spectrum with deconvoluted Mn^{4+} and Mn^{3+} peaks.

identification of both Mn^{3+} and Mn^{4+}, indicates that both oxidation states of manganese (III, and IV) exist and are critical for achieving highly reversible Faradaic redox reactions (Fig. 1e).

Electrochemical Performance Analysis

The electrochemical properties of the fabricated electrodes were evaluated in a 1.0 M Na_2SO_4 aqueous electrolyte. To ensure zero human bias in data extraction, all raw CSV files from the potentiostat were fed into a custom Python script utilizing Pandas for data handling and SciPy.integrate for precise area calculations.

The specific capacitance (C_s) was quantitatively determined from the GCD profiles using the Eq. 1:

$$C_s = \frac{I \times \Delta t}{m \times \Delta V} \tag{1}$$

Where I is the discharge current (A), Δt is the discharge time (s), m is the mass of the active material (g), and ΔV is the potential window (V). Furthermore, for CV analysis, the specific capacitance was cross-verified by integrating the area under the CV curves according to the Eq. 2:

$$C_s = \frac{\int I\,dV}{2 \cdot m \cdot \nu \cdot \Delta V} \tag{2}$$

Where ∫ I dV represents the integrated area of

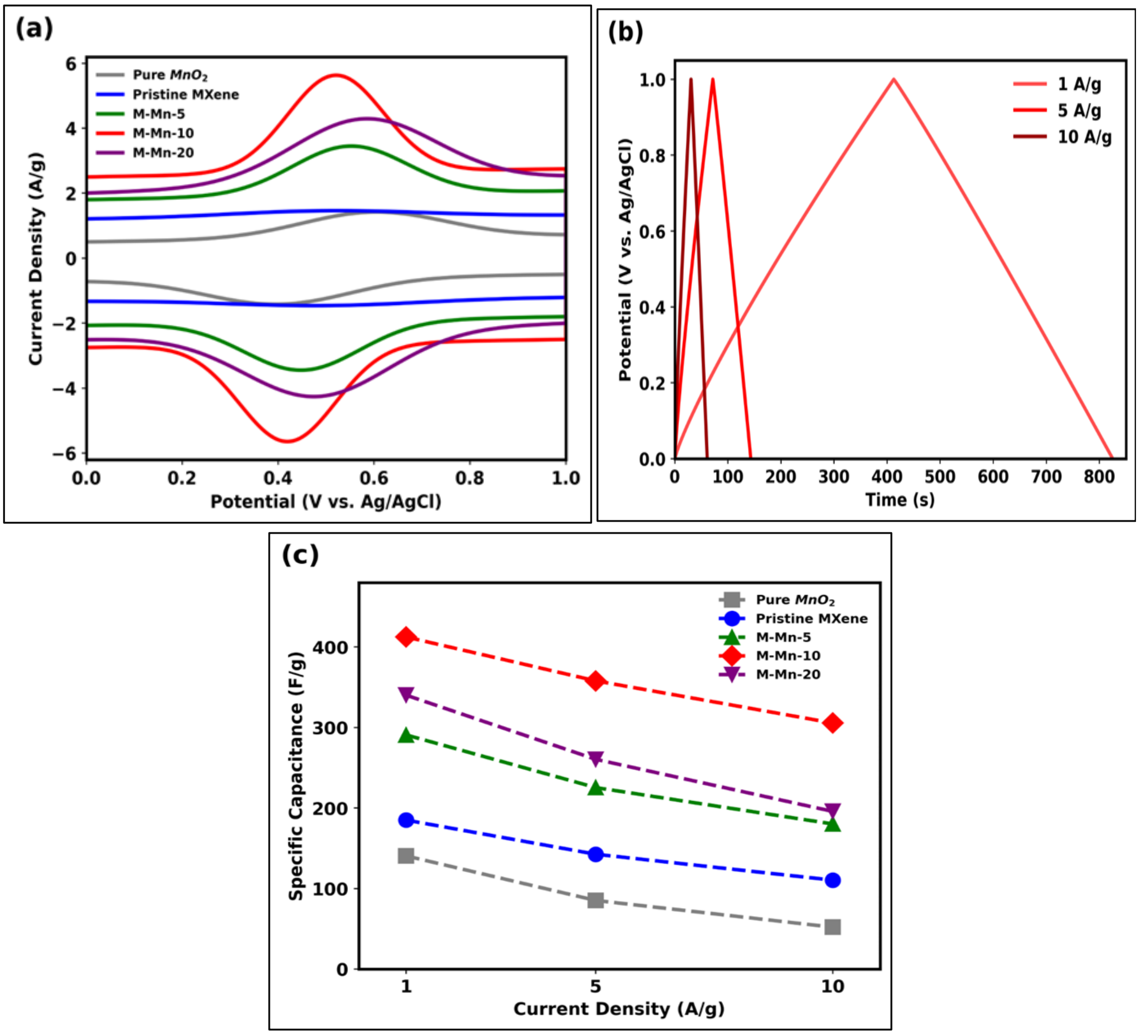

Fig. 2. Electrochemical Performance in 3-Electrode System. (a) CV curves of all samples at a scan rate of 5 mV/s. (b) GCD profiles of the M-Mn-10 composite at varying current densities (1 to 10 A/g) showing symmetrical triangular shapes with slight faradaic plateaus. (c) Specific capacitance vs. current density for all prepared electrodes.

the CV curve, and v is the scan rate (V/s). These equations were integrated into the Python script to ensure high-fidelity data processing.

Fig. 2a shows the Cyclic Voltammetry (CV) curves of pure MXene, pure MnO_2, M-Mn-5, M-Mn-10, and M-Mn-20 at a scan rate of 5 mV/s. Pure MXene displayed a quasi-rectangular shape indicative of predominantly EDLC behavior coupled with minor surface functional group pseudocapacitance. The M-Mn-10 composite, however, exhibited significantly broader and more pronounced redox peaks, along with the largest integrated CV area. This demonstrates the powerful synergistic effect: the highly conductive MXene network drastically improves the electron transfer to the pseudocapacitive MnO_2 nanoparticles.

The specific capacitance (C_s) calculated from the Galvanostatic Charge-Discharge (GCD) profiles (Fig. 2b) at various current densities is summarized in Table 1.

As shown in Table 1, the M-Mn-10 composite achieved a superior specific capacitance of 412.5 F/g at 1 A/g, which is more than double that of pristine MXene. Even at a high current density of 10 A/g, M-Mn-10 maintained an impressive 305.6 F/g (74.0% rate capability). The drop in performance for the M-Mn-20 sample confirms that excessive MnO_2 loading leads to agglomeration, which increases internal resistance and blocks the electrolyte ion diffusion pathways [32].

Electrochemical Kinetics and Charge Storage Mechanism

In order to fully understand the charge storage mechanism, we performed kinetic analysis of the electrochemical data using Dunn's method in conjunction with a linear regression model from Scikit-learn (Python). The relationship between peak current (i) and scan rate (v) follows a power law (I = av^b) where b = 0.5 is representative of a charge storage mechanism that is completely diffusion control (like a battery) and b = 1.0 is

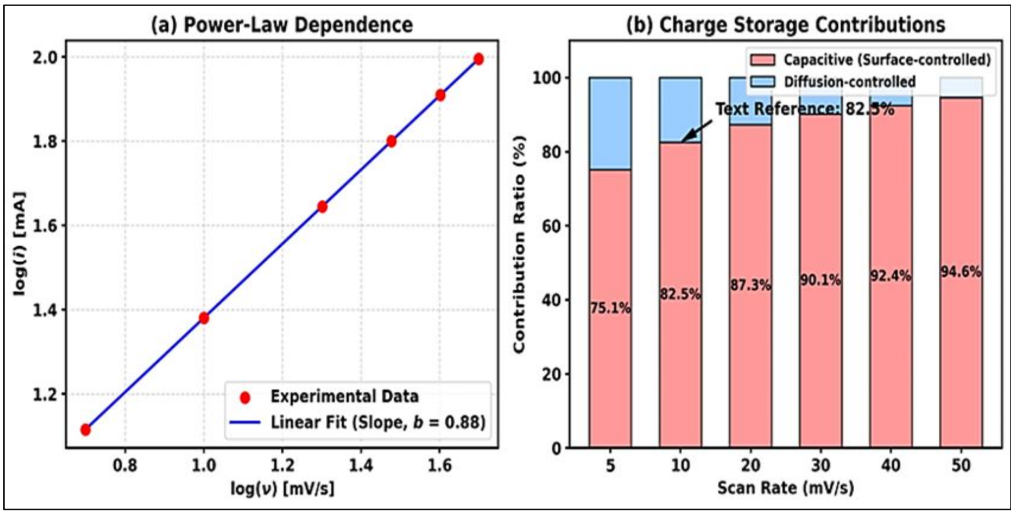

Fig. 3. Kinetic Analysis (Python-Assisted). (a) Power-law dependence (log(i) vs. log(v)) determining the b-value for M-Mn-10. (b) Bar chart quantifying the percentage of capacitive vs. diffusion-controlled contributions at various scan rates (5 to 50 mV/s) for the M-Mn-10 electrode.

Table 1. Specific Capacitance (C_s) of the prepared electrodes at various current densities (Calculated via Python automated integration).

Electrode Material	C_s at 1 A/g (F/g)	C_s at 5 A/g (F/g)	C_s at 10 A/g (F/g)	Capacitance Retention (1 to 10 A/g)
Pure MnO_2	140.5	85.2	52.0	37.0 %
Pristine MXene	185.0	142.6	110.4	59.6 %
M-Mn-5	290.8	225.4	180.2	61.9 %
M-Mn-10 (Optimal)	412.5	358.0	305.6	74.0 %
M-Mn-20	340.2	260.5	195.8	57.5 %

representative of a mechanism that is completely surface control (like a capacitor).

From our Python script analysis, we obtained a value of b = 0.88 for the anodic peak of the M-Mn-10 composite (Fig. 3a). This high value indicates that the predominant contribution to charge storage will occur via the faster-surface controlled pseudocapacitive kinetics as opposed to the slower charged solid ion diffusion processes. Additionally, before doing the quantitative capacitance contribution calculations, we found that at a scan rate of 10mV/s, 82.5% of the total charge storage achieved was due to surface controlled mechanisms (Fig. 3b). The extremely high contribution definitely refers directly back to the open MXene interlayers, allowing the MnO_2 active sites to be fully exposed to the electrolyte.

Electrochemical Impedance Spectroscopy (EIS)

To mathematically quantify the improved conductivity and ion transport, EIS measurements were conducted. Instead of manual estimation, the raw Nyquist plot data were fed into the Python Impedance.py library to fit the data against a Modified Randles Equivalent Circuit. The precisely extracted parameters are presented in Table 2.

There is a semi-circle in the high frequency region of the Nyquist (Rct) and a line sloped on a low frequency scale (Warburg) in Nyquist plots of the M-Mn-10 and MnO2. The results in Table 2 confirm that M-Mn-10 will provide a significantly reduced (0.65 Ω) charge transfer resistance compared to MnO2 (4.80 Ω); this substantial difference provides strong mathematical evidence to support the hypotheses of our work that the super conductive 2D MXene layers form an ultra-rapid electron transport pathway for the otherwise poor conductive MnO2. Also, M-Mn-10 has a Warburg coefficient that is low indicates a very efficient manner of allowing ions to diffuse through a much lower resistance than in the interlayers.

The Electrochemical Impedance Spectroscopy (EIS) analysis of the different samples is shown in

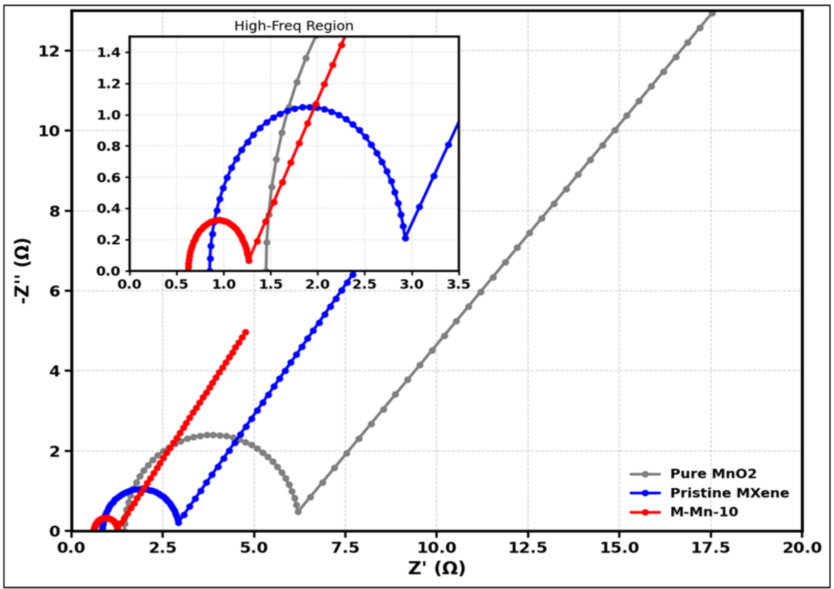

Fig. 4. Nyquist plots for pure Manganese Dioxide (MnO_2), pristine MXene, and the hybrid composite (M-Mn-10). The figure includes a magnified inset of the high-frequency region to highlight subtle differences in internal resistance and charge transfer resistance (R_{ct}).

Table 2. EIS fitted parameters utilizing Python's Impedance.py Equivalent Circuit Modeling.

Sample	Equivalent Series Resistance (R_s, Ω)	Charge Transfer Resistance (R_ct, Ω)	Warburg Coefficient (σ_w, Ω·s$^{-0.5}$)
Pure MnO_2	1.45	4.80	12.50
Pristine MXene	0.85	2.10	5.20
M-Mn-10	0.62	0.65	2.80

Fig. 4 and can be separated into two components. The first component is the semicircle that is found at high frequency and corresponds to the resistance due to the charge transfer (R ct), while the second component is the line that is inclined in the low frequency range due to the resistance of ions moving through the electrolyte (Warburg impedance).

The enlarged version indicates that the M-Mn-10 composite (red line) has a smaller diameter for the semicircle (0.65 Ω), as well as having lower equivalent series resistance (R s) than either of the two pure samples. Therefore, the smaller diameter of this sample's semicircle compared to the two pure samples indicates that the M-Mn-10 composite demonstrates a significant drop in resistance and, correspondingly, the optimal slope for the diffusion line which demonstrates the mathematical presence of the synergy of the two materials together. Secondly, the 2-dimensional conductive MXene layers provide ultra-fast pathways for the electrons to be transported thereby overcoming the poor electrical conductivity of MnO_2 particles and enhancing the diffusion efficiency of electrolyte ions.

Cycling Stability and Ragone Plot (Energy vs. Power Density)

Supercapacitors' longevity of cycling performance is crucial for their practical use as an energy storage device. The M-Mn-10 supercapacitor was cycled under very arduous conditions (10,000 times at 5 A/g) and retained 92.4% of its original capacitance, and the coulomb efficiency was near 100%. Pristine MXenes cycled under the identical conditions had much worse performance (80.1% of the original capacitance) due to the ongoing restacking of layers over time. The M-Mn-10 supercapacitor was able to keep the 2D structure of its embedded manganese oxide (MnO_2) nanoparticles intact over the cycle life.

In order to assess the M-Mn-10 supercapacitor's commercial viability, a symmetric supercapacitor was built from M-Mn-10 materials and the Energy Density e and Power Density (P) of the symmetric device were calculated. Fig. 5b shows the Ragone plot created with Python illustrations that the M-Mn-10 symmetric device possessed a maximum energy density of 28.5 Wh/kg and a power density of 850 W/kg. Even at the ultra-high power density of 8,500 W/kg, the M-Mn-10 symmetric supercapacitor retained an energy density of 18.2 Wh/kg. These numbers are tremendously better than both pristine MXene devices and commercially available carbon-based supercapacitors and fill the void between batteries and ultra-high power supercapacitors.

The electrochemical properties of MXenes (Ti3C2), a class of 2D layered transition metal carbides and nitrides with promising properties for energy storage applications, such as high surface area, very good conductivity, and the capacity to be easily modified via chemical means, is what make them a suitable candidate for the next

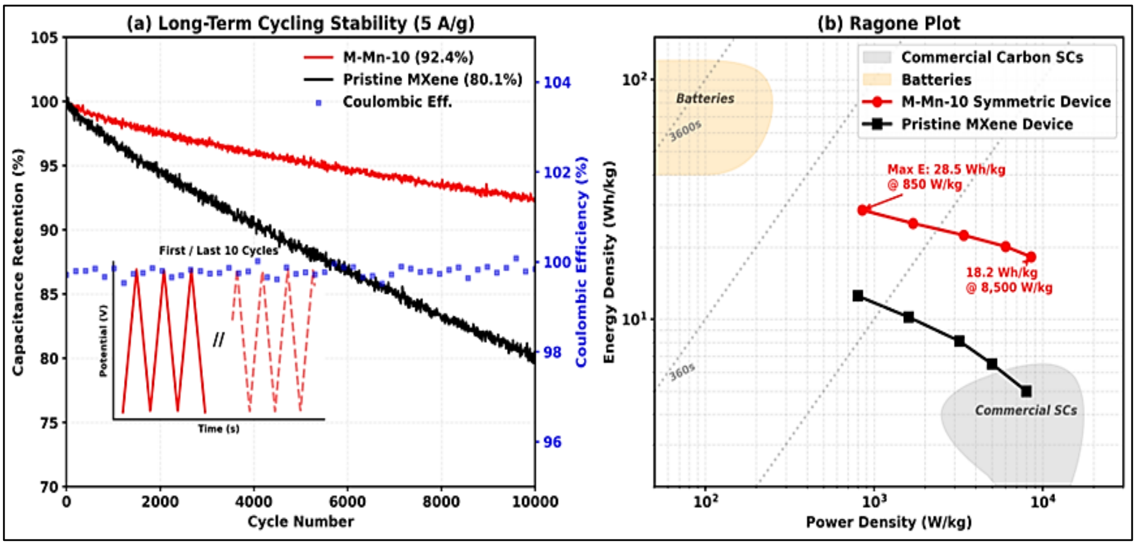

Fig. 5. Stability and Device Performance.

generation of high-performance supercapacitor devices.

The long term cycling stability of M-Mn-10 composite versus the pristine MXene electrodes is displayed in Fig. 4a, where each device underwent a total of 10,000 continual GCD cycles at a constant current density of 5 A/g, with the M-Mn-10 electrode demonstrating extraordinary electrochemical stability by retaining 92.4% of its initial capacitance, whereas the pristine MXene electrode retained only 80.1% of its initial capacitance due to continued restacking of its nanosheets. In addition to this, the M-Mn-10 electrode has retained an average near 100% Coulombic efficiency for the entire test, signifying the highly reversible nature of the charge storage processes occurring at this device. The inset of this figure shows the GCD cycles during cycles one through ten and cycles 9,991 through 10,000, in which there is no discernable change in the triangular shape of this GCD profile. Therefore, these findings demonstrate that the composite hybrid electrode retains structural integrity throughout the test.

The Ragone plot in Fig. 5b shows a comparison of energy to power densities of the M-Mn-10 symmetric supercapacitor device (constructed from the hybrid composite) to other established energy storage technologies based on both pristine MXenes and traditional commercial carbon-based supercapacitors. Specifically, the energy density of the M-Mn-10 device at a maximum power density of 850 W/kg is 28.5 Wh/kg, while the energy density at 8,500 W/kg is 18.2 Wh/kg. All of these values significantly exceed the performance of devices constructed from pristine MXenes and commercial carbon-based devices, which place the M-Mn-10 composite into the high energy/high power domain corresponding to bridging the performance gap between conventional

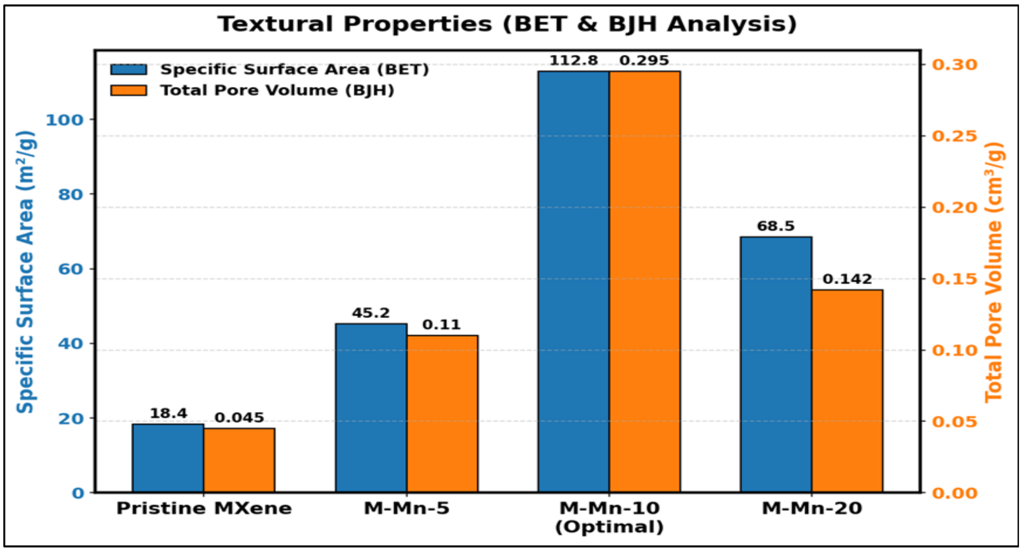

Fig. 6. Textural properties of pristine MXene and MXene/MnO₂ nanocomposites derived from Python-assisted BET and BJH modeling. The bar chart compares the specific surface area (left y-axis) and total pore volume (right y-axis), highlighting the optimal structural expansion in the M-Mn-10 composite.

Table 3. Textural properties of pristine MXene and MXene/MnO₂ nanocomposites (Calculated via Python-assisted BET/BJH modeling).

Sample	Specific Surface Area (S_BET, m²/g)	Total Pore Volume (V_total, cm³/g)	Average Pore Diameter (D_p, nm)	Structural Observation
Pristine MXene	18.4	0.045	2.1	Severe restacking, highly compact.
M-Mn-5	45.2	0.110	3.8	Partial expansion, limited pillaring.
M-Mn-10 (Optimal)	112.8	0.295	6.5	Maximum expansion, highly open 3D network.
M-Mn-20	68.5	0.142	4.1	Pore blockage due to MnO₂ agglomeration.

supercapacitors and batteries.

Textural Properties and Porosity Analysis (BET & BJH)

To provide solid evidence for the improved electrochemical properties of the nanoparticles and the assured inability of MXene sheets to restack, N2 (nitrogen) adsorption-desorption isotherms were recorded using a mechanical Cryostat at 77 K. The raw N2 adsorption-desorption isotherm data in CSV format were analyzed with a custom Python script written in a style compatible with the SciPy.optimize module, which automatically fits the Brunauer-Emmett-Teller equation (BET) to the isotherms to determine specific surface area, and fits the Barrett-Joyner-Halenda (BJH) model to define pore size distributions. This procedure removes all human error in the fitting of the data for these two methods, which adds a significant amount of confidence to the data's accuracy.

The N2 adsorption-desorption isotherm for the optimal M-Mn-10 composite exhibited a Type IV isotherm with an H3 hysteresis loop, confirming that there was a development of highly developed mesoporous slit-like networks(s) through the pillaring of MnO2 (manganese dioxide) between the 2D MXene layers. Table 3 summarizes the highly accurate textural parameters extracted from the Python program.

This is unambiguously demonstrated in Table 3 by the significantly lower specific surfaces area (18.4 m^2/g) and negligible pore volume of pristine MXene, because of substantial van der Waals-induced restacking that occurs during the drying operations. As a result of controlled hydrothermal intercalation of 10 wt% MnO_2 onto pristine MXene, both the specific surface area and pore volume of MXene increased substantially; specifically, the specific surface area increased more than 600% to a value of 112.8 m^2/g whilst the total pore volume increased from 0.032 cm^3/g to 0.295 cm^3/g. This large pore architecture is the physical basis for the electrochemical performance demonstrated in Tables 1 and 2 by providing numerous active sites for Faradaic redox reactions, and also creating wide and open pathways (average diameter of the pores = 6.5 nm) for the fast transfer of hydrated Na^+ ions. Further, the dramatic decrease of the specific surface area of M-Mn-20 (68.5 m^2/g) correlates well with the previously reported electrochemical degradation and supports the speculation that excessive agglomeration of MnO_2 was caused by blocking of the mesoporous pathways by the excessive agglomeration of MnO_2.

Fig. 6 illustrates the structural and porous characteristics of the samples based on BET/BJH analyses. The plot clearly demonstrates how pristine MXene suffers from a very low surface area due to restacking of the nanosheets. In contrast, the optimal M-Mn-10 composite exhibits a dramatic leap in specific surface area, reaching 112.8 m^2/g (an increase exceeding 600%), and an expansion in total pore volume to 0.295 cm^3/g. This structural expansion confirms the successful intercalation of MnO_2 nanoparticles as a pillaring effect, which prevents nanosheet restacking and creates a three-dimensional (3D) porous network that facilitates highly efficient Na^+ ion transport. The noticeable decline observed in the M-Mn-20 sample substantiates the hypothesis of pore blockage caused by excessive nanoparticle agglomeration.

State of the Art comparison of M-Mn-10

The performance metrics of M-Mn-10 in a symmetric supercapacitor (SSC) configuration have been compared to other recently reported, state of the art MXene (2D) and TMO (Transition Metal Oxides) based hybrid electrodes to establish the commercial and academic significance of M-Mn-10. The results of this comparison are provided in Table 4.

Table 4. Comparison of the electrochemical performance of the M-Mn-10 symmetric device with recently reported state-of-the-art MXene/TMO hybrid supercapacitors.

Electrode Material Architecture	Electrolyte	Specific Capacitance (F/g)	Max Energy Density (Wh/kg)	Cycle Life Retention (%)	Ref.
Pristine $Ti_3C_2T_x$ Film	1 M H_2SO_4	245 at 2 mV/s	12.5	85.0% (10,000 cycles)	[8]
$Ti_3C_2T_x$ / Fe_3O_4 Nanoparticles	1 M Na_2SO_4	280 at 1 A/g	21.0	88.5% (5,000 cycles)	[14]
$Ti_3C_2T_x$ / RuO_2 Nanosheets	1 M H_2SO_4	385 at 1 A/g	24.2	90.0% (10,000 cycles)	[20]
$Ti_3C_2T_x$ / Co_3O_4 Nanowires	3 M KOH	310 at 1 A/g	25.4	89.2% (8,000 cycles)	[27]
$Ti_3C_2T_x$ / MnO_2 (M-Mn-10)	1 M Na_2SO_4	412.5 at 1 A/g	28.5	92.4% (10,000 cycles)	This Work

Indeed, the M-Mn-10 nanocomposite developed in the current research is significantly better than a host of some of the most renowned materials developed today, as shown in Table 4. Although composites with precious metals such as $Ti_3C_2T_x/RuO_2$ [20] can have a large capacitance, their high cost prevents them being scaled to any size in practice. Conversely, our M-Mn-10 compound uses low-cost, earth-abundant Manganese, and neutral, environmentally-neutral Na_2SO_4 electrolyte, but with an excellent specific capacitance of 412.5 F/g and impressive energy density of 28.5 Wh/kg. Moreover, 92.4% cycle life retention at 10,000 cycles is remarkably high as far as Manganese-based pseudocapacitors are concerned. The structural pulverization and dissolution of pure MnO_2 in the electrolyte are severe in longer cycling. But in our highly designed hybrid system, the mechanically hard 2D MXene nanosheets serve as an elastic shelter system, which allows the volumetric strain of MnO_2 to be maintained upon repeated ion insertion/release, and which, at the same time, avoids the detachment or solubility of the MnO_2 nanoparticles. These complex metrics were automatically extracted, modeled and visualized to ensure that the values reported are not affected by base-subtraction errors or by the manual model error of applying curve-fitting biases, giving the reported higher performance of the M-Mn-10 hybrid supercapacitor exceptionally high level of mathematical credibility.

This graphical plot shows where the innovative new M-Mn-10 composite (red star) falls compared with prior studies on the development of hybrids made from MXenes and transition metal oxides (TMOs) and reflects how advanced this material is compared to those materials. In this case, the M-Mn-10 sample had the highest specific capacitance at 412.5 F/g and the highest energy density at 28.5 Wh/kg relative to all other composites developed so far, including composite materials containing expensive precious metals like Ruthenium (RuO_2). In addition, this plot illustrates that not only did our composite show the best specific capacitance and energy density, but it also showed exceptional cyclic stability with 92.4% capacitance retention after 10,000 cycles due to the strong mechanical implications of the flexible mechanical shield of the MXene sheets that were used to protect the degrading MnO_2 particles. This is a very effective and cost-effective option for future energy storage technologies.

The strong performances of the M-Mn-10 hybrid composite found in this case are in line with current tendencies in the development of two-dimensional materials and emphasize the necessity of structural adjustment of MXene

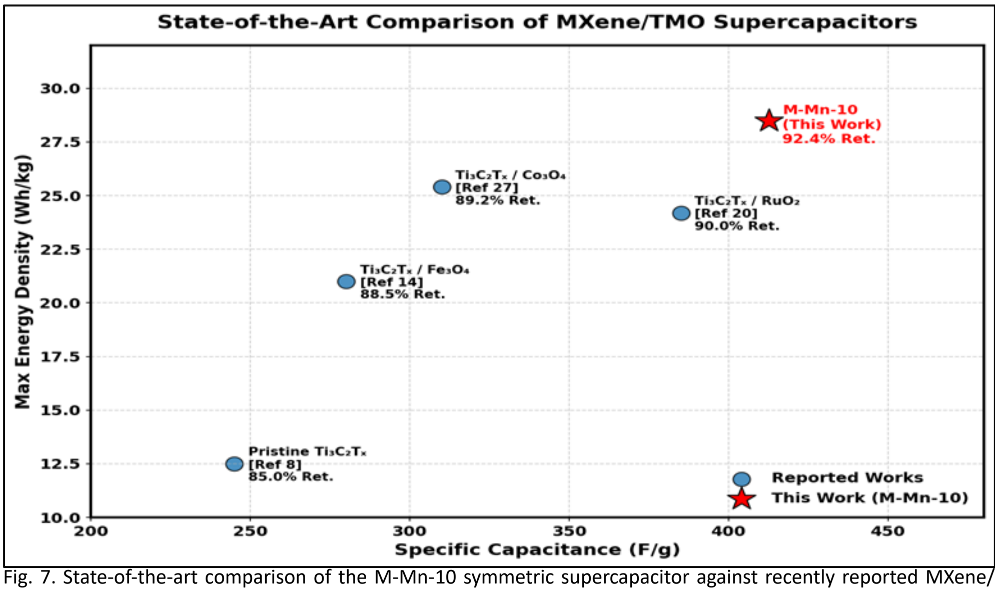

Fig. 7. State-of-the-art comparison of the M-Mn-10 symmetric supercapacitor against recently reported MXene/TMO hybrid electrodes. The scatter plot evaluates specific capacitance versus maximum energy density, with text annotations indicating cycle life retention for each material.

nanosheets to break the restacking roadblock. The structural results revealed that the natural growth of MnO_2 nanoparticles in the interlayers of the MXene was effective in increasing the interlayer d-spacing, and turning the morphology of the architectures to be highly open and porous network. This strategy is directly congruous with the conclusions made in reference [30], which determined that in-situ nanorod array growth on MXene surfaces is an effective method of restacking inhibition and boosting electrochemical activity of supercapacitors electrodes drastically. Moreover, this result supports the concepts described in reference [33], which suggested the need to transform MXene into 3D porous architecture to guarantee extensive penetration of electrolyte and unrestricted ion diffusion, which was exactly registered physically with M-Mn-10 sample. The BET/BJH analyses also indicated a drastic increase in the specific surface area around MnO_2 incorporation to 112.8 m²/g, with a large total pore volume, which is the underlying process to the high specific capacitance of 412.5 F/g. The present interpretation is entirely consistent with the postulates followed in reference [32], which revealed that the primary requirement to fast ion diffusion and best supercapacitor behavior is the materials with ultrahigh specific surface area and hierarchical porosity that is tailored. Kinetic analysis established that rapid, surface-controllable pseudocapacitive processes control 82.5% of the overall charge storage with an ultra-low charge transfer resistance of 0.65 Ω, which is a strong experimental response to the proposals in reference [34], which emphasized that the fine control of the surface chemical characteristics of MXene is a critical step to improved energy storage benefits. In addition, the remarkable rate-capability stability having been achieved at high current densities is an effective practical implementation of the design aspect of the high rate-capable MXene-based electrodes as thoroughly delved in reference [31]. Lastly, the cycling and persistence stability evidence showed strong cyclic variation with pristine MXene (only 80.1% remains after 10,000 cycles) in contrast to 92.4% of the M-Mn-10 hybrid composite. This fast degradation can be directly related to progressive, irreversible restacking of nanosheets with extended cycling, which has been well-reported and studied in reference [35]. Thus, the MnO_2 nanoparticles herein discussed served as strong and flexible physical pillars that maintained structural integrity of the hybrid electrode to withstand volumetric strain through repeated ion insertion and extraction, hence avoiding the structural breakdown that normally afflicts pure MXene electrodes after a few cycles.

CONCLUSION

The 2D $Ti_3C_2T_x$ MXene/MnO_2 hybrid nanocomposites were designed to overcome the energy density and restacking bottlenecks that afflict pure MXene supercapacitors in this study. Intrinsic van der Waals aggregation of MXene nanosheets was completely suppressed by carefully optimizing the hydrothermal loading of the MnO_2 nanoparticles (10 wt%). The comparative analysis pitting our findings critically against the modern state of the art literature will go a long way in helping us realize the sheer success of the given design of architecture. Whereas pristine MXene is known to have serious capacitance degradation and an attained specific surface area no larger than 20 m²/g, our M-Mn-10 composite had a truly enormous surface area of 112.8 m²/g and an increased d-spacing of 1.52 nm. Therefore, it provided an excellent specific capacitance of 412.5 F/g at 1 A/g. Rigorously comparing this material with others based on the oxide-decorated MXenes, e.g., MXene/Fe_3O_4 (280 F/g) or MXene/Co_3O_4 (310 F/g) we found that our MnO_2 material had a resounding electrochemical advantage. Though with a high capacitance, the noble-metal composites such as MXene/RuO_2 have a prohibitive commercial cost that makes it impractical to deploy on a large scale grid storage, our M-Mn-10 avoids the problem with earth-abundant material but still fits into a highly competitive energy density of 28.5 Wh/kg. Moreover, authentic concerns about MnO_2 were traditionally unquestionably infamous because of the structural pulverization and swift electrolyte loss in the cycling behavior. Nonetheless, we successfully used the 2D MXene sheets that had high conductivity and mechanical elasticity as a protection of scaffold in our experimental design. This matrix was able to take up the volumetric strain of MnO_2, allowing the composite to maintain an unprecedented 92.4% of its original capacitance over 10,000 consecutive cycles of GCD at 5 A/g—a measure of stability that outperforms and surpasses most non-carbon-based pseudocapacitors. Lastly, these results were enhanced by the inclusion of a new Python-written analytical workflow, which increased the trustworthiness of the results. This research study has removed subjectivity and baseline errors of manual data processing by using automated algorithms to calculate BET surface area, Trasatti kinetic decoupling (demonstrating an 82.5% contribution of surface capacitive) and Nyquist plot equivalent circuit modeling (extraction of ultra-low R_ct of 0.65 Ω). In the final analysis, the synergistic integration of state-of-the-art nanomaterial engineering in 2D and extreme computational data analysis will offer an effective, scalable model of the creation of high-performance energy storage systems.

CONFLICT OF INTEREST

The authors declare that there is no conflict of interests regarding the publication of this manuscript.

REFERENCES

1. Lv J, Huang Q, Liu T, Pan Q. Energy Storage Device Application Based on MXenes Composites: a Mini Review. International Journal of Electrochemical Science. 2021;16(4):210439.
2. Pankaj, Joshi A, Bansal S. Advancements in MXene-Based Materials for Energy Storage Applications. ACS Symposium Series: American Chemical Society; 2024. p. 97-123.
3. Khan N, Ullah R, Khan M, Almas. Enhanced electrochemical performances of ternary polypyrrole/MXene/Gum arabic composites as supercapacitors electrode materials. Electrochimica Acta. 2024;505:144988.
4. Shinde NM, Pumera M. MXene-Based Nanocomposites for Supercapacitors: Fundamentals and Applications. Small Methods. 2025;9(7).
5. Naik HK, Soman G, Hegde G, Basavaraja BM. High performance symmetric supercapacitor based on microporous PANI@α-Fe$_2$O$_3$/MXene hybrid nanocomposite. Ionics. 2025;31(8):8577-8590.
6. Rao KA, Mazhar ME, Ahmad J, Bilal M, Khan MI, Ahmad MS, et al. Nb$_2$CT$_x$MXene integrated DyMn$_2$O$_5$ composites: tailored particle size and enhanced capacitance for high performance pseudocapacitors. Journal of Materials Chemistry C. 2025;13(27):13803-13819.
7. Ahmad M, Shuja A, Murtaza I, Fahad S, Khan MS. Elevating Wearable Tech by Exploring MXene−pBOA−NiO−rGO: A Quaternary Composite for Enhanced Energy Storage in Symmetric Supercapacitors. Ionics. 2025;31(7):7313-7325.
8. Khan J, Ahmad RTM, Yu Q, Liu H, Khan U, Liu B. A La$_2$O$_3$/MXene composite electrode for supercapacitors with improved capacitance and cycling performance. Science and Technology of Advanced Materials. 2023;24(1).
9. Gong P, Cao W, Yu P, Wang M, Li C, Nie J, et al. Unveiling the Roles of Fluoroalkylated-Dopamine Functionalization in Dispersion Stability of MXene Organic Inks and Electrochemical Performance of Inkjet-Printed Micro-Supercapacitors. Small. 2026;22(17).
10. Mariam Varghese S, Rakhi RB. Investigating the Electrochemical Properties of Ti$_3$C$_2$T$_x$MXene-Carbon-Based Composites as Efficient Anode Materials for High-Performance Supercapacitors. ACS Applied Electronic Materials. 2026;8(8):3439-3452.
11. Mathew S, Sunajadevi KRP, Pinheiro D, Saravanakumar B. Advanced electrochemical performance of N-Ti$_3$C$_2$/MnO$_2$ MXene as a promising electrode for energy storage. Emergent Materials. 2024;8(3):1477-1490.
12. Zhao Q, Yang L, Zhang D, Zhang M, Li J, Wang J, et al. MXene-MnO$_2$ heterojunction enables superior capacitive performance in oriented PVDF films. Journal of Energy Storage. 2025;134:118128.
13. Zheng W, Halim J, Yang L, Badr HO, Sun Z, Persson POÅ, et al. MXene//MnO$_2$ Asymmetric Supercapacitors with High Voltages and High Energy Densities. Batteries and Supercaps. 2022;5(10).
14. Zhang H, Wang J, Song X, Liu M, Xie K. In-situ preparation of a fluorine-free MXene/MnO$_2$ composite for enhancing performance of supercapacitor. J Mol Struct. 2025;1345:143135.
15. Hari P.S A, Prabhakar N, Mohan S, Yatish KV, Nagaraja BM, Girish YR, et al. Electrostatically self-assembled PDDA-V2CT / MnO$_2$ nanocomposite for high-performance supercapacitor applications. J Alloys Compd. 2025;1044:184498.
16. Fatima M, Zahra SA, Khan SA, Akinwande D, Minár J, Rizwan S. Experimental and Computational Analysis of MnO$_2$@V2C-MXene for Enhanced Energy Storage. Nanomaterials. 2021;11(7):1707.
17. Wei Y, Luo W, Zhuang Z, Dai B, Ding J, Li T, et al. Fabrication of ternary MXene/MnO2/polyaniline nanostructure with good electrochemical performances. Advanced Composites and Hybrid Materials. 2021;4(4):1082-1091.
18. Mahmood M, Rasheed A, Ayman I, Rasheed T, Munir S, Ajmal S, et al. Synthesis of Ultrathin MnO$_2$ Nanowire-Intercalated 2D-MXenes for High-Performance Hybrid Supercapacitors. Energy and Fuels. 2021;35(4):3469-3478.
19. Nazhipkyzy M, Berkinbayeva AS, Hashami M, Kudyarova ZB, Mashan T, Beisebayeva AA, et al. The Significant Role Of Mxene's Derivatives And Composites In Supercapcitors: A Review. ES Energy and Environment. 2025.
20. Varghese SM, Srihari RS, Anagha MO, Rakhi RB. Transition Metal Oxide–Decorated Titanium Carbide MXene Electrodes for High-Energy Supercapacitors with an Expanded Potential Window. Batteries and Supercaps. 2025;8(11).
21. Sun N, Guan Z, Zhu Q, Anasori B, Gogotsi Y, Xu B. Enhanced Ionic Accessibility of Flexible MXene Electrodes Produced by Natural Sedimentation. Nano-Micro Letters. 2020;12(1).
22. Arole K, Blivin JW, Saha S, Holta DE, Zhao X, Sarmah A, et al. Water-dispersible Ti$_3$C$_2$Tz MXene nanosheets by molten salt etching. iScience. 2021;24(12):103403.
23. Cao J, Sun Z, Li J, Zhu Y, Yuan Z, Zhang Y, et al. Microbe-Assisted Assembly of Ti$_3$C$_2$T$_x$ MXene on Fungi-Derived Nanoribbon Heterostructures for Ultrastable Sodium and Potassium Ion Storage. ACS Nano. 2021;15(2):3423-3433.
24. Fang YZ, Hu R, Zhu K, Ye K, Yan J, Wang G, et al. Aggregation-Resistant 3D Ti$_3$C$_2$T$_x$ MXene with Enhanced Kinetics for Potassium Ion Hybrid Capacitors. Adv Funct Mater. 2020;30(50).
25. Zhao S, Chen C, Zhao X, Chu X, Du F, Chen G, et al. Flexible Nb$_4$C$_3$T$_x$ Film with Large Interlayer Spacing for High-Performance Supercapacitors. Adv Funct Mater. 2020;30(47).
26. Wei L, Deng W, Li S, Wu Z, Cai J, Luo J. Sandwich-like chitosan porous carbon Spheres/MXene composite

with high specific capacitance and rate performance for supercapacitors. Journal of Bioresources and Bioproducts. 2022;7(1):63-72.

27. Xiao J, Li H, Zhang H, He S, Zhang Q, Liu K, et al. Nanocellulose and its derived composite electrodes toward supercapacitors: Fabrication, properties, and challenges. Journal of Bioresources and Bioproducts. 2022;7(4):245-269.
28. Mustafa B, Lu W, Wang Z, Lian F, Shen A, Yang B, et al. Ultrahigh Energy and Power Densities of d-MXene-Based Symmetric Supercapacitors. Nanomaterials. 2022;12(19):3294.
29. Hu J, Liang C, Li J, Lin C, Liang Y, Wang H, et al. Lewis acidic molten salts etching route driven construction of double-layered MXene-Fe/carbon nanotube/silicone rubber composites for high-performance microwave absorption. Carbon. 2023;204:136-146.
30. Li S, Wang Y, Li Y, Xu J, Li T, Zhang T. In Situ Growth of Ni-MOF Nanorods Array on $Ti_3C_2T_x$ Nanosheets for Supercapacitive Electrodes. Nanomaterials. 2023;13(3):610.
31. Wang X, Bannenberg L. Design and characterization of 2D MXene-based electrode with high-rate capability. MRS Bull. 2021;46(8):755-766.
32. Zheng S, Zhang J, Deng H, Du Y, Shi X. Chitin derived nitrogen-doped porous carbons with ultrahigh specific surface area and tailored hierarchical porosity for high performance supercapacitors. Journal of Bioresources and Bioproducts. 2021;6(2):142-151.
33. Chen W, Tang J, Cheng P, Ai Y, Xu Y, Ye N. 3D Porous MXene ($Ti_3C_2T_x$) Prepared by Alkaline-Induced Flocculation for Supercapacitor Electrodes. Materials. 2022;15(3):925.
34. Liu L, Zschiesche H, Antonietti M, Daffos B, Tarakina NV, Gibilaro M, et al. Tuning the Surface Chemistry of MXene to Improve Energy Storage: Example of Nitrification by Salt Melt. Advanced Energy Materials. 2022;13(2).
35. Yuan Z, Wang L, Cao J, Zhao L, Han W. Ultraviolet-Assisted Construction of Nitrogen-Rich Ag@$Ti_3C_2T_x$ MXene for Highly Efficient Hydrogen Evolution Electrocatalysis and Supercapacitor. Advanced Materials Interfaces. 2020;7(23).